

Final Draft
of the original manuscript:

Bachurin, D.V.; Nazarov, A.A.; Weissmueller, J.:
Grain rotation by dislocation climb in a finite-size grain boundary
In: Acta Materialia (2012) Elsevier

DOI: [10.1016/j.actamat.2012.09.014](https://doi.org/10.1016/j.actamat.2012.09.014)

GRAIN ROTATION BY DISLOCATION CLIMB IN A FINITE-SIZE GRAIN BOUNDARY

D.V. Bachurin ^{a,b}, A.A. Nazarov ^b, J. Weissmüller ^{c,d}

^a Institut für Angewandte Materialien, Karlsruher Institut für Technologie (KIT), Karlsruhe, Germany

^b Institute for Metals Superplasticity Problems, Russian Academy of Science, Ufa, Russia

^c Institut für Werkstoffphysik und Werkstofftechnologie, Technische Universität Hamburg-Harburg, Hamburg, Germany

^d Institut für Werkstoffforschung, Werkstoffmechanik, Helmholtz-Zentrum Geesthacht, Geesthacht, Germany

ABSTRACT

We investigate the kinetics of grain rotation in a bicrystal with a tilt grain boundary by studying the relaxation of an edge dislocation wall in a discrete-dislocation approach. The boundary is infinitely extended in one direction and of finite size in the orthogonal one. The relaxation process is simulated numerically by solving the equations of motion of the dislocations, assuming climb by diffusive transport in the boundary plane. Surprisingly, we find that boundaries never rotate all the way into coincidence. Instead, the final state is a metastable array with 18 dislocations and, hence, with a finite misorientation that depends on the boundary length and the Burgers vector. All boundaries with fewer than 18 dislocations are also metastable. The relaxation time to reach the metastable configuration is found proportional to the logarithm of the number of dislocations and to the cube of the length of the boundary. We give a critical discussion of image force arguments that underlie earlier work on grain rotation, and verify that the present analysis of image forces does satisfy the boundary conditions at the free surfaces. The results have implications for the kinetics of rotation of nanoparticles on a substrate and for the stability of grain and subgrain boundaries in thin metal films.

Keywords: Grain boundary; Grain rotation; Dislocation; Recovery; Micromechanical Modelling

1. INTRODUCTION

The dependency of the energy of a grain boundary on the misorientation between the lattices of the abutting crystals results in a torque which, given an appropriate kinetics, lets the crystallites rotate towards a low-energy orientation or coincidence [1-5]. Grain rotation experiments, such as the sphere-on-a-plate technique, have used this process to identify low energy orientations [6-12]. Grain rotation is also of relevance to sintering [6], where it reduces the grain boundary energy and, hence, the driving force for densification. Recently, there has been a renewed interest in grain rotation with relation to microstructures with very small grains: it is believed that grain rotation contributes significantly to grain growth as well as to plastic deformation of polycrystalline materials with a nanometer grain size. This notion rests on the considerable acceleration of the rate of rotation when the grain size, D , is reduced. In polycrystals, where the rotation requires accommodation of the grain shape, so that its rate is limited by the process of plastic deformation in the bulk rather than by the processes in the boundary, the rotation rate has been predicted to scale with D^{-4} [4,13,14]. Indeed, computer simulations of grain growth confirm a decisive contribution of rotation [15], which may be coupled with grain boundary migration [16]. The deformation processes in nanocrystalline materials, of high interest in the field of metal plasticity, are also linked to grain rotation, even when metals are deformed at low homologous temperatures. Computer simulations showing rotation during plastic deformation of nanocrystalline metals [17] are supported by experimental observations of large deformation without the development of noticeable texture [18] and by *in-situ* transmission electron microscopy [19].

In spite of the present interest in the issue, the microscopic processes behind grain rotation are not completely understood, nor are general predictions for the dependency of the rotation rate on grain size and misorientation available. Here, we inspect the final stage of the rotation, when there is only a small deviation from coincidence (small-angle boundary) or from a low-energy orientation (boundary which is vicinal to a low- Σ orientation). The boundary can then be described as an array of individual dislocations, and the rotation rate analyzed in terms of the motion of the grain boundary dislocations driven by their elastic interaction. At first sight, one might object that this is the least relevant part of the process. This is suggested by the following argument. Near coincidence or special orientations, the specific boundary energy γ is believed to exhibit cusps where it varies logarithmically with an appropriate misorientation angle, θ . According to the Read-Shockley equation [20],

$$\gamma = \gamma_0 \theta (A - \ln \theta), \quad (1)$$

where γ_0 is a constant which depends on the elastic properties of the material and A is a constant which depends on the core energy of an individual dislocation. As a consequence of Eq. (1), the torque, $\partial\gamma/\partial\theta$, diverges when the misorientation angle θ becomes small. The final stage of the rotation, at small θ , might then be fast, and the actual rotation rate might be expected as controlled by the slower rotation at larger angles. Remarkably, this expectation is not born out by previous investigations of the untilting or untwisting of grain boundaries at sinter necks. Cahn [21] as well as King and Balasubramanian [22] find a slowing down of the rotation as coincidence is approached. Molecular dynamics simulations of nanoclusters on a substrate even point towards situations where the rotation stops altogether before coincidence can be reached [23]. Cahn [21] points out that the driving force argument, which links $d\theta/dt$ to $\partial\gamma/\partial\theta$, is not forceful. The rotation involves a sequence of discrete events, the absorption of dislocations at the triple lines which bound the neck. Immediately after an absorption event, the new leading dislocation is comparatively far from the neck and experiences a small climb

force. Thus, long periods of slow relaxation intervene between the absorption events, and the resulting rotation rate depends decisively on the atomistic processes in the neck, on top of the driving force from $\partial\gamma/\partial\theta$.

One might think of another objection against an uncritical acceptance of the driving force argument using Eq. (1). The Read-Shockley equation is derived for infinitely extended boundaries, and in the absence of data or theory for finite-size boundaries a smooth (for instance, quadratic) θ -dependence of γ cannot be ruled out in the limit where the boundary contains only few dislocations. This would contrast with the cusp-scenario of extended boundaries, and would provide an alternative explanation for the slow rotation into coincidence.

The considerations above emphasize the interest in understanding the untilting of small-angle boundaries, and it has lead us to re-inspect the problem, with attention to the effect of finite boundary length. Surprisingly, we find that the relaxation not only slows down at small misorientation, but that a metastable state with finite misorientation is reached when the number of dislocations in the boundary drops down to a specific, small number. Independently of the size of the neck, this number is 18 dislocations. Thus, our results suggest that the rotation never continues all the way to coincidence, but that it will always be arrested at a finite misorientation.

The paper is organized as follows: we start out (Section 2) with a critical examination of the concept of discrete image dislocations, which has been used in previous work [22,24,25]. We then (Section 3) apply the concept of virtual images, which goes back to work by Marcinkowski [26,27] and has been applied to thin films by Gutkin and Romanov [28] and by Vladimirov, Kolesnikova and Romanov [29]. In Section 4, we discuss the equations of motion for the particular case of dislocation climb limited by grain boundary diffusion. This is followed by validation of the equations and by a display and discussion of the results of a numerical simulation of the rotation, Sections 5 and 6.

2. PRELIMINARY CONSIDERATIONS

2.1 Geometry

Grain rotation can be of relevance in various scenarios which will a priory require separate treatment. Plastic deformation creates a torque on an individual grain in a polycrystal, and the corresponding rotation requires that sliding occurs simultaneously on all the boundaries connecting the grain to its neighbours. Similarly, the sum of the torques from $\partial\gamma/\partial\theta$ on all boundaries of a given grain will not generally cancel, so that there is a driving force for rotation even when there is no deformation. Besides grain boundary sliding, grain rotation in a polycrystal requires that a separate process provides for accommodation of the grain shape, for instance diffusive transport of matter along grain boundaries or plastic deformation of the grain interior. An analysis of grain rotation in a polycrystal will therefore require consideration of mechanisms or constitutive laws of grain boundary sliding, as well as a discussion of the prevailing accommodation mechanism. While first experimental data for sliding are emerging [30], both issues are far from being resolved. This applies specifically in the interesting limit of very small grain size. We find it instructive to consider the relevant special case of the untilting of a small-angle tilt boundary bounded by free surfaces, since it allows for a discussion of grain rotation separately from sliding and accommodation. Furthermore, the established structural description of small-angle boundaries in terms of arrays of lattice dislocations provides a simple approach to the energetics and kinetics of rotation.

Figure 1 illustrates dislocation arrays in finite-size tilt grain boundaries. For a boundary in a sinter neck (Fig. 1a), three interaction terms are relevant for grain rotation:

- i).* the mutual repulsion between pairs of dislocations in an array gives rise to a line force which tends to drive the outermost dislocations out of the neck, a process which reduces the dislocation content and, thereby, the misorientation angle.
- ii).* the image forces are expected to attract each dislocation to the nearest surface.
- iii).* where the dislocation intersects the triple line which bounds the neck, a point force results from the coupling between the position of the intersection point and the dislocation line length. This force acts to displace the intersection point along the triple line, thereby reducing the dislocation line length and energy.

On the circular neck, all three driving forces will typically cooperate to promote the rotation towards coincidence.

A simpler situation ensues when a small-angle grain boundary is infinitely extended in one dimension, as in the tilt boundary in a thin film depicted in Fig. 1b. Here, the rotation is due exclusively to the first two of the above forces. In the interest of a traceable solution we restrict attention to this situation and consider exclusively tilt boundaries. An additional incentive is that a manageable solution to the image force problem is known for this geometry.

We consider a small-angle symmetric tilt grain boundary which is infinitely extended in the direction of the tilt axis, but of finite length $L = 2h$ in the direction normal to that (Fig. 1b). The two crystals meeting at the boundary are considered to be semi-infinite planar sheets of thickness L , their lattice orientations are allowed to differ by a (small) angle θ , and the boundary normal is taken to be in the plane of the sheets. The boundary can then be described by an array of dislocations, with their Burgers vector - of magnitude b_0 - normal to the boundary plane. For the time being, we take the dislocations to have identical spacing Δ . Let us assume an array of $2n_0$ dislocations labelled by i . We then have

$$\theta = b_0 / \Delta = b_0 n_0 / h. \quad (2)$$

We use orthonormal coordinate axis with 'x' normal to the sheet surface and 'z' along the intersection of the boundary and sheet planes.

The climb force per line length on any given dislocation is given by $b_0 \sigma_{yy}$, where σ denotes the stress at the position of the dislocation. Given sufficient mobility, the dislocations will climb under the effect of their interactions with each other and with the surfaces. As the outermost pair of dislocations reaches the surface, they pop out and disappear. The process ends when the last dislocation has popped out and the two grains rotated into coincidence. Modelling the climb requires in the first instance a description of the stress field - specifically the stress component σ_{yy} - of a finite array of dislocations in a grain boundary bounded by free surfaces.

The stress field of each individual dislocation depends not only on the nature and position of the dislocation but also on the boundary conditions at the free surfaces. If - as we assume - there are no external forces, equilibrium requires that the stress components σ_{xx} , σ_{xy} , and σ_{xz} must vanish everywhere on the surface. Furthermore, $\text{div}\boldsymbol{\sigma} = 0$ in the bulk at equilibrium. Since simple analytical expressions for the stress field of a single dislocation in an infinite solid (which satisfies $\text{div}\boldsymbol{\sigma} = 0$) are known, it is convenient to use these expressions as the basis functions in a decomposition of the net stress. The actual stress in the finite solid is then

represented as the superposition of such basis functions, centered at the positions of the actual dislocations and at those of extra, ‘image’ dislocations outside the solid.

2.2 The ‘discrete image dislocation’ approach

It has been suggested that an appropriate stress field for the finite-size boundary is obtained with an infinite array of image dislocations, of periodicity $2L$, located in the extension of the boundary plane [22]. In this picture, when the neck dislocations are at positions x_i , then there are images at positions $x_{i,m}^* = \pm(mL + x_i)$, $m = 1, 2, \dots$, where the sign of their Burgers vector is identical (opposite) to that of the neck dislocations if m is even (odd). Here, the task of each m -th set of images is to compensate the stress components of the $(m-1)$ -st set at one of the surfaces. By inspection it is readily seen that, in this way, one can indeed achieve a vanishing net stress σ_{xy} at both surfaces. However, it is also readily found that at the same time the component σ_{xx} is actually doubled when the images are introduced. Therefore, the stress field obtained with the image dislocation array does not satisfy the boundary conditions.

The failure of the image dislocation approach is well known for the case of dislocations in a half space. In that geometry, the correct σ_{xx} and σ_{xy} are obtained with an added stress function which produces no stress at the position of the dislocation [31]. The discrete image approach then gives an exact description of the force on the dislocation. Yet, it is not obvious how the approach can be transferred to the thin film geometry, where the added stress function – as derived for the half-space – would violate the boundary condition at the second surface. In the following section we shall make use of a different approach to image forces, which does satisfy the boundary conditions.

3. STRESS FIELDS OF DISLOCATIONS IN A THIN FILM

The stress field of a straight edge dislocation placed parallel to the surfaces in a thin solid film has been analyzed in Ref. [28], using again an image dislocation approach. The images are here not discrete dislocations but rather a continuous distribution, and they are located at the free surfaces, not along the extended boundary plane. The problem treated in Ref. [28] is actually more general than the present one, since the original grain boundary dislocation may have a Burgers vector of arbitrary orientation, and since the film is allowed to consist of two layers with independent elastic parameters. In spite of the simplification introduced by the present geometry (uniform elastic response, restriction to Burgers vectors normal to the boundary plane and to the stress values in the plane, see Fig. 1b), the expressions for the stress fields remain awkward and require numerical integration. Vladimirov et al. [29] have previously applied the analysis of Ref. [28] to a uniform thin film, restricting attention to a single dislocation. These authors found that climb forces do not necessarily attract the dislocation to the film surface. In this section we present the analysis and generalize it to arrays of several dislocations. By means of examples, we verify that the resulting stresses satisfy the boundary conditions.

3.1 Stress field of a single dislocation

The method of Ref. [28] goes back to an approach originally introduced by Marcinkowski and coworkers [26,27]. Two distributions of virtual edge dislocations are placed at each free

surface, one each with the Burgers vector in x direction and in y direction, respectively. The dislocation densities are adjusted so as to satisfy the boundary conditions at the surface. The equilibrium equation in the bulk is also satisfied, since the bulk stress field of each virtual dislocation satisfies $\text{div } \mathbf{S} = 0$.

As above, we consider a thin film which is infinitely extended in the y - and z - direction and of thickness $L = 2h$. The dislocation is situated at a distance d from the central plane of the film. The Burgers vector, \mathbf{b}_0 , is normal to the boundary plane (i.e., along y) and the dislocation line is along z . We write $\sigma(d,x,y)$ for the value, at position (x,y) , of the stress tensor due to a dislocation located at position d , and we require that

$$\sigma_{xj}(d, \pm h, y) = 0, \quad (3)$$

where $j = x,y$ labels stress components normal (x) and tangential (y) to the surface.

The two surface virtual dislocation arrays (two Burgers vector orientations) are denoted by indices $1x, 1y$ for the surface at $x = h$ and $2x, 2y$ for the surface at $x = -h$. The notation of Ref. [28] denotes the corresponding image dislocation densities in the arrays by f^{1x}, f^{1y} and f^{2x}, f^{2y} , and multiplies them by infinitesimal Burgers vectors b_x (the x -component) and b_y (the y -component) (Fig. 2). Any physically meaningful statements will always depend on products of the form $f^{ij}b_j$ – representing a Burgers vector content per area of surface – and never on f^{ij} or b_j alone. The values of the b_j are thus arbitrary, and we here use the convention $b_x = b_y = b$, which greatly simplifies the notation.

In Ref. [28], the solution of the problem satisfying the boundary conditions, Eq. (3), has been found in the following form:¹

$$\sigma_{ij}(d, x, y) = \sigma_{ij}^0(d, x, y) + \sigma_{ij}^v(d, x, y), \quad (4)$$

where $\sigma_{ij}^0(d, x, y)$ refers to the stress field of an edge dislocation in an infinite uniform medium [32], and where the terms $\sigma_{ij}^v(d, x, y)$ represent the net stress field of all virtual dislocations. We have

$$\sigma_{ij}^v(d, x, y) = \int_{-\infty}^{\infty} e^{isy} \sum_{\substack{k=1,2 \\ l=x,y}} \Phi^{kl}(s) \tilde{\sigma}_{ij}^{kl}(x, s) ds, \quad (5)$$

where the indices k and l label the virtual dislocation arrays, $k = 1,2$ and $l = x,y$. The fields $\tilde{\sigma}_{ij}^{kl}(x, s)$ are the Fourier transforms of the fields $\sigma_{ij}^{kl}(x, y - y')$ caused by the virtual dislocations from the arrays with the densities f^{kl} ; s is the coordinate in the Fourier space. All Fourier transforms of all components of stress fields have been calculated in Ref. [28].

The unknown functions $\Phi^{kl}(s)$ are Fourier transforms of the distribution functions of the virtual dislocations and can be found from the system of algebraical equations

$$B_p(d, s) = C_{pr}(s) \Phi_r(d, s), \quad (6)$$

where summation convention applies, where Φ is the vector

$$\Phi = \left(\Phi^{1x}(d, s) \quad \Phi^{1y}(d, s) \quad \Phi^{2x}(d, s) \quad \Phi^{2y}(d, s) \right),$$

¹ The equations in Ref. [28] are set up for a more general case which requires a distinction between two half spaces, denoted by upper left indices. In the present context, all equations take on the same form for the regions of positive and negative x . We can therefore drop the upper left indices of the original reference.

and where the functions $C_{pr}(s)$ and $B_p(d,s)$ are known and also have been calculated in Ref. [28].

Consistent with the geometry under study, we apply the equations of Ref. [28] to the special case where the shear modulus, G , and Poisson ratio, ν , are uniform and where the Burgers vector is parallel to the film surface, specifically $\mathbf{b}_0=(0, -b_0, 0)$. The coefficients used in Ref. [28] will then take on the following values: elastic uniformity coefficient $\Gamma=1$; $k_1 = k_2 = 3 - 4\nu$; $A = (1 - \Gamma)/(1 + k_1\Gamma) = 0$, $\tilde{B} = (k_2 - k_1\Gamma)/(k_2 + \Gamma) = 0$, $A' = (\Gamma - 1)/(k_2 + \Gamma) = 0$ and $\tilde{B}' = (k_1\Gamma - k_2)/(1 + k_1\Gamma) = 0$; $D = G/(4\pi(1 - \nu))$ with G the shear modulus and ν Poisson's number.

In order to evaluate climb forces, one needs to calculate the stress component σ_{yy} in the plane of the boundary (i.e., at $y = 0$). This stress is a sum of the stresses due to the individual dislocations in the wall. Taking into consideration all assumptions made above and using Eq. (4), σ_{yy} at position x due to a dislocation at position d can be written as follows:

$$\sigma_{yy}(d, x, 0) = \sigma_{yy}^0(d, x, 0) + \int_{-\infty}^{\infty} \sum_{kl} \Phi^{kl}(d, s) \tilde{\sigma}_{yy}^{kl}(x, s) ds, \quad (7)$$

where

$$\sigma_{yy}^0(d, x, 0) = -2Db_0/(x - d). \quad (8)$$

The Fourier transforms of the fields in Eq. (7) are

$$\tilde{\sigma}_{yy}^{1x}(x, s) = D b \sqrt{2\pi} i \operatorname{sgn}(s) e^{-|s(x-h)|} (1 + |s|(x - h)), \quad (9a)$$

$$\tilde{\sigma}_{yy}^{1y}(x, s) = D b \sqrt{2\pi} e^{-|s(x-h)|} (|s|(h - x) - 2), \quad (9b)$$

$$\tilde{\sigma}_{yy}^{2x}(x, s) = D b \sqrt{2\pi} i \operatorname{sgn}(s) e^{-|s(x+h)|} (1 - |s|(x + h)), \quad (9c)$$

$$\tilde{\sigma}_{yy}^{2y}(x, s) = D b \sqrt{2\pi} e^{-|s(x+h)|} (|s|(x + h) - 2). \quad (9d)$$

The $\Phi^{kl}(s)$ in Eq. (7) can be obtained from equation (6), using the functions $C_{pr}(s)$ and $B_p(d, s)$ in the following form:

$$C_{11}(s) = C_{22}(s) = C_{33}(s) = -C_{44}(s) = D b \sqrt{2\pi} i \operatorname{sgn}(s), \quad (10a)$$

$$C_{21}(s) = C_{12}(s) = 0, \quad (10b)$$

$$C_{31}(s) = C_{13}(s) = D b \sqrt{2\pi} i \operatorname{sgn}(s) e^{-2h|s|} (2h|s| + 1), \quad (10c)$$

$$C_{41}(s) = C_{14}(s) = C_{32}(s) = -C_{23}(s) = -D b \sqrt{2\pi} e^{-2h|s|} 2h|s|, \quad (10d)$$

$$C_{43}(s) = C_{34}(s) = 0, \quad (10e)$$

$$C_{42}(s) = -C_{24}(s) = -D b \sqrt{2\pi} i \operatorname{sgn}(s) e^{-2h|s|} (2h|s| - 1), \quad (10f)$$

$$B_1(d, s) = D b_0 e^{-|s|(h-d)} |s|(h - d), \quad (10j)$$

$$B_2(d, s) = D b_0 i \operatorname{sgn}(s) e^{-|s|(h-d)} (1 - |s|(h - d)), \quad (10h)$$

$$B_3(d, s) = -D b_0 e^{-|s|(h+d)} |s| (h+d), \quad (10i)$$

$$B_4(d, s) = -D b_0 i \operatorname{sgn}(s) e^{-|s|(h+d)} (|s| (h+d) - 1). \quad (10j)$$

Computing the stress on a dislocation by Eq. (7) involves, as the first step, inverting Eq. (6) to obtain the vector Φ . This is straightforward by exploiting Eqs. (10), and yields Φ in closed form. The results, in combination with Eq. (9) for the $\tilde{\sigma}_{yy}^{kl}$, yields the kernel of the integral in Eq. (7). In the absence of a closed-form solution for the integral, numerical evaluation was required. This evaluation is simplified by combining the integration at $q < 0$ with that at $q \geq 0$. Equation (7) is thereby transferred to the following form:

$$\sigma_{yy}(d, x, 0) = \sigma_{yy}^0(d, x, 0) + \frac{D b_0}{h} \int_0^{\infty} K(\delta, \varepsilon, q) dq \quad (\text{for } x > 0), \quad (11a)$$

and

$$\sigma_{yy}(d, x, 0) = \sigma_{yy}^0(d, x, 0) - \frac{D b_0}{h} \int_0^{\infty} K(-\delta, -\varepsilon, -q) dq \quad (\text{for } x < 0). \quad (11b)$$

As above, σ_{yy}^0 is given by Eq. (8), and the kernel, K , obeys

$$K(\delta, \varepsilon, q) = \frac{2e^{q(1-\delta)}}{1 + e^{8q} - 2e^{4q}(1 + 8q^2)} \times \{ e^{q(-1+\varepsilon)} [q(1 + q(-1 + \varepsilon)) A_1 + (-2 + q - q\varepsilon) A_2] + e^{-q(1+\varepsilon)} [(-2 + q + q\varepsilon) A_3 + q(-1 + q + q\varepsilon) A_4] \} \quad (12)$$

with

$$A_1 = -1 + e^{2q(3+\delta)}(-1 + \delta) + \delta + e^{2q(1+\delta)}(1 - \delta + 4q(1 + \delta)) - e^{4q}(-1 + \delta + 4q(1 + \delta)), \quad (13a)$$

$$A_2 = 1 + q + e^{2q(3+\delta)}(1 + q(-1 + \delta)) - q\delta + e^{4q}(-1 - 4q^2(1 + \delta) + q(3 + \delta)) - e^{2q(1+\delta)}(1 + 4q^2(1 + \delta) + q(3 + \delta)), \quad (13b)$$

$$A_3 = e^{2q}(1 - q(-3 + \delta) - 4q^2(-1 + \delta)) + e^{2q(2+\delta)}(1 + q(-3 + \delta) - 4q^2(-1 + \delta)) + e^{6q}(-1 + q + q\delta) - e^{2q\delta}(1 + q + q\delta), \quad (13c)$$

$$A_4 = e^{2q}(-1 + 4q(-1 + \delta) - \delta) + e^{6q}(1 + \delta) + e^{2q\delta}(1 + \delta) - e^{2q(2+\delta)}(1 + 4q(-1 + \delta) + \delta), \quad (13d)$$

and with the reduced dislocation position variable, $\delta = d/h$, the reduced spatial coordinate for the point at which the stress is computed, $\varepsilon = x/h$, and the coordinate in reduced Fourier space, $q = sh$. The numerical integration of Eq. (7) yields the yy -component of the stress field of a dislocation including the image stress. This is a central part of our analysis.

3.2 Array of dislocations

For an array of several dislocations in the boundary plane, the stress acting on i -th disloca-

tion located in the region $x > 0$ is calculated by summing of the stresses induced by the individual dislocations. The summation can be written as follows:

$$\sigma_{yy}^i = \sigma_{yy}^v(d = x_i, x_i, 0) + \sum_{\substack{j=1 \\ j \neq i}}^n \sigma_{yy}(d = x_j, x_i, 0) + \sum_{j=1}^n \sigma_{yy}(d = -x_j, x_i, 0). \quad (14)$$

The first term on the right-hand side of Eqn. (14) embodies the image stress of the i -th dislocation as in Eqn. (5). The remaining terms represent the stresses from all other dislocations (except the i -th one) located in the regions of positive and negative x , respectively. These latter stresses, which combine the direct and image stresses, are given by Eq. (7).

3.3 Numerical computation of the stress fields

For each dislocation configuration, the stress acting on any given dislocation is obtained by numerical integration of Eqs. (11a) or (11b). The integration is well conditioned, in particular since the kernel decays exponentially at large q . This approach was used, in particular, to compute the stresses on single dislocations and on dislocations pairs as presented in Section 5.1 below.

A modified approach was selected for the analysis of the dislocation kinetics. Here, in order to calculate the stress value at any point on the boundary plane, one must sum up the stresses from different dislocations, i.e. for several couples of variables d and x . Direct calculation of these stresses at each simulation step slows down the simulations drastically. It is more convenient to use stress tables which contain the values of the stress for a certain mesh in the two-dimensional space made by the variables d and x . We used this approach, with the mesh size adjusted in dependence of h , in the range from $h / 40$ to $h / 320$ for both variables. The stress tables contained from 3321 to 205761 values. To compute the stresses in the intermediate points lying between the mesh nodes in which these stresses are known, a two-dimensional linear interpolation method has been used.

4. EQUATIONS OF MOTION FOR THE DISLOCATIONS

In order to follow the dislocation motion in the boundary in a numerical simulation, one needs to relate the climb force - see the previous section - to the climb velocity. To this end we use an analysis by Arzt et al. [33], which considers climb mediated by vacancy diffusion along the boundary plane. The dislocation cores and the free surfaces are taken as ideal sinks and sources for vacancies. Dislocations move by absorption or emission of vacancies. The local chemical potential at the sources and sinks is considered at equilibrium, subject to the normal stress. Hence, $\mu = \mu_0 + \sigma_{yy} \Omega$, where Ω denotes the atomic volume [33]. Net vacancy fluxes arise from differences in the stress at the individual dislocation cores, which entail differences in μ . The resulting equation for the climb velocity is [33]

$$\frac{dx_i}{dt} = \frac{\delta \mathcal{D}_b \Omega}{b_0 kT} \left(\frac{\sigma_{yy}^{i+1} - \sigma_{yy}^i}{x_{i+1} - x_i} - \frac{\sigma_{yy}^i - \sigma_{yy}^{i-1}}{x_i - x_{i-1}} \right), \quad (15)$$

for $i = 1, 2, \dots, n-1$, where σ_{yy}^i denotes the normal stress at the core of i -th dislocation and $\delta \mathcal{D}_b$ refers to the grain boundary diffusion coefficient, the product of an apparent bulk diffusion coefficient \mathcal{D}_b in a layer at the grain boundary and an apparent grain boundary thickness δ

[34]. Equation (15) has been used previously in problems similar to the present one, specifically the relaxation kinetics of extrinsic dislocation walls (disclination dipoles and disclination quadrupoles) in deformed polycrystals [35,36].

When writing the motion equation for the head dislocations ($i = n$), it is essential to keep in mind the boundary condition for the chemical potential at the surfaces, which act as sinks or sources for vacancies. Since vacancies are generated at equilibrium, we have $\mu = \mu_0$ at the surface. Therefore, the equation (15) for $i = n$ can be written in the following way:

$$\frac{dx_n}{dt} = \frac{\delta \mathcal{D}_b \Omega}{b_0 k T} \left(\frac{0 - \sigma_{yy}^n}{h - x_n} - \frac{\sigma_{yy}^n - \sigma_{yy}^{n-1}}{x_n - x_{n-1}} \right). \quad (16)$$

By inspection of equation (15) it is seen that the kinetics of the relaxation depend on the materials parameters via $\delta \mathcal{D}_b \Omega / b_0 k T$. Furthermore, the stresses depend on $G b_0 / 4\pi(1-\nu)$. In the numerical computation we find it convenient to introduce a characteristic time, t_0 , which depends on the materials parameters and on the boundary length according to

$$t_0 = t_1 \frac{h^3}{b_0^3}. \quad (17)$$

with t_1 only dependent on the material,

$$t_1 = \frac{4\pi(1-\nu)kT}{\delta \mathcal{D}_b G} \frac{b_0^3}{\Omega}, \quad (18)$$

and to use the dimensionless time, $\tau = t / t_0$. Furthermore, we use dimensionless position coordinates, $\tilde{x}_i = x_i / h$. Then the equations are written in a simple form $d\tilde{x}_i / d\tau = F_i$, where the F_j are dimensionless combinations of the stresses and coordinates similar to those in the brackets of equation (15).

Equation (15), which determines the kinetics in our study, relates the vacancy flux to the driving forces via the grain boundary diffusion constant. Yet, the dislocation climb in the small-angle tilt grain boundaries that are the primary object of our study involves vacancy diffusion through the crystal lattice in-between the dislocations. It appears then more appropriate to replace \mathcal{D}_b with the (typically much smaller) bulk diffusion coefficient and δ with an effective diffusion cross-section in the bulk. In grain boundaries of mixed character, which require two intersecting sets of dislocations, pipe diffusion through one set may short-circuit the bulk diffusion, leading to accelerated climb in the other. By specifying the results for the relaxation kinetics in terms of the normalized time τ , we adopt a form that is independent of the choice of the diffusion coefficient.

5. RESULTS OF THE SIMULATION

5.1 Validation

By means of validation, Fig. 3 illustrates the stress fields (including the image stresses) of a single dislocation. The boundary conditions require that the normal stress component, σ_{xx} , vanishes at the free surface. The examples in the figure consider the dislocation located in the central plane of the film (Figs. 3a and 3b) and mid-way between that plane and the free surface (Fig. 3c). The stresses in the plane $y = h$ (Fig. 3b) were calculated using Eq. (5) taking

$y = h$ in the exponent. Note, that $\Phi(s)$ and $\sigma(x,s)$ in Eq.(5) do not depend on y . For comparison, the figure also shows the stresses that are obtained when image stresses are ignored. At the surface, these stresses deviate noticeably from zero, violating the boundary conditions. By contrast, our results for the image stress are seen to indeed satisfy the boundary conditions with good accuracy. This supports the validity of the model of Ref. [28] and verifies its implementation in our work.

Figure 4 shows the variation of the climb force, $\sigma_{yy} b_0$, per line length on a single dislocation as it approaches a free surface of the film. Also shown is the climb force obtained by the classic image force model as discussed in Section 2.2. The two expressions disagree in the interior of the film, but it is apparent that they converge in the limit where the distance from the surface is much less than the film thickness. In that limit, the present results are therefore consistent with the well-established solution for a dislocation in a half space.

5.2 Climb forces and energy for simple configurations

We now inspect the climb force in more detail, focussing initially on the simple configuration of a single dislocation in a thin film of half thickness h . Figure 5a shows the magnitude of the climb force per line length plotted versus the position, d , of the dislocation. The result agrees with a previous analysis of the same configuration, see Fig. 4 in Ref. [29]. In agreement with expectation, the image forces drive dislocations in the *outer* regions of the film to climb towards the surface. Remarkably, however, dislocations in the *inner* half of the film are driven towards the centre. In other words, the image forces attract the dislocation to the surface if and only if it is closer to the surface than some critical position $d = 0.54h$. Farther away from the surface, the direction of the image force is inverted, and the dislocation is repelled. All forces are balanced in the film centre ($d = 0$), which represents a metastable position for the dislocation, with energy barriers preventing the egression from the film. The points $d^{us} = \pm 0.54h$ represent unstable equilibrium configurations.

It is of interest to consider the variation of the elastic energy of the dislocation with position. That energy is conventionally obtained as the work which is done against the image forces when transferring the dislocation from the free surface into its current position [32]. The divergence of the stress in the immediate vicinity of the surface requires the introduction of a cut-off radius, which can be adjusted so that the dislocation core-energy is correctly represented. Once the film thickness is sufficiently large compared to the extension of the dislocation, the cut-off and the core-energy will be independent of h . In other words, the cut-off introduces a new length-scale into the problem, obliterating the scaling relations that emerge from the analysis presented in Sections 3 and 4. In order to separate out that issue, we specify all energies relative to the value in the metastable state.

The graph of energy versus position in Fig. 5b, obtained as described above, illustrates the presence of the metastable equilibrium state. In the interest of discussing specific grain boundary energy, γ , we find it appropriate to refer the elastic energy of the dislocation arrays to the area of the grain boundary. This convention is adopted here, even though a single dislocation does not represent a properly formed small-angle grain boundary. In Fig. 5b we thus specify $\Delta\gamma = \gamma(d) - \gamma_{\text{metastable}}$.

Figure 6 analyzes the case of two dislocations, confined to symmetric arrangement with positions at $+d$ and $-d$, respectively. Without lack of generality we inspect, in Fig. 6a, the im-

age forces on one of the dislocations. The figure also shows the direct (bulk) repulsive forces (ignoring the image forces) and the net force, combining both contributions. It is seen, that all forces are of comparable magnitude. In spite of the repulsive direct interaction, there are regions in which the net force repels the dislocations from the surface. There remains a metastable configuration, with the dislocations located at positions $x_1^{ms} \approx \pm 0.38h$. An unstable equilibrium is reached at $x_1^{us} \approx \pm 0.74h$.

The graphs of Figs. 5 and 6 illustrate the scaling of the stresses and energies. The stresses required to drive the dislocations out of their metastable equilibrium states are in the order of Db_0/h . This value diminishes as the boundary width h is increased, indicating that smaller applied stresses would be required to overcome the energy barrier and untilt the boundary. The same statement holds for the specific (grain boundary) energy $\Delta\gamma$ in the unstable state. For a given number of dislocations, this energy barrier height scales with Db_0^2/h . In this sense the metastable state emerges as more robust for smaller boundaries.

5.3 Relaxation kinetics

We investigated boundaries containing $2n_0$ dislocations with a uniform initial spacing, $\Delta = h/n_0$ (Fig. 2). The head dislocations were initially at a distance $\Delta/2$ from the free surfaces. The initial misorientation obeys Eq. (2). We have followed the motion of the dislocations during grain rotation, assuming a mirror symmetry centre in the middle of the film; otherwise, each pair was allowed to relax freely subject to the forces and kinetics described above. Specifically, the velocities were obtained by Eqs. (15), applying numerical integration via the second-order Runge-Kutte method. When the head dislocations reach the surface, they are assumed to disappear, and n_0 is decreased by 1, then the process is repeated with $n_0 - 1$ dislocation pairs. In that way the relaxation could be followed until the last dislocation vanished at the surface, so that coincidence was reached. We have found that there are two different types of dislocation behaviour depending on the initial number of dislocation pairs in the wall: the case when $n_0 \leq 18$ and $n_0 > 18$. Both cases will be considered separately below.

5.3.1 Case of $n_0 \leq 18$

The climb forces for the case of one dislocation pair, $n_0 = 1$, have been discussed above. Here, dislocations climb from their initial positions $x_1 = \pm 0.5h$ towards the center of the film and stop at the metastable equilibrium points. Dislocations can reach the free surfaces only if they start out from positions outside of (i.e., closer to the surface than) the unstable equilibrium points. Conversely, when starting out inside the unstable equilibrium points, the dislocations will climb to the metastable equilibrium points. A similar behaviour is found for $n_0 = 2$ through 10. Starting our from the equidistant initial positions as described above, all dislocations climb inwards until a metastable array with positions x_i^{ms} is reached. When the leading dislocations (i.e. those which are located closest to the free surfaces) are displaced “by hand” to positions outside a certain limiting value while keeping the other dislocations in their positions, the leading dislocations relax towards the surfaces and egress. The remaining dislocations then rearrange towards new metastable equilibrium points $x_i^{ms'}$. For example, the metastable equilibrium points for $n_0 = 2$ are $x_1^{ms} \approx \pm 0.22h$, $x_2^{ms} \approx \pm 0.64h$ and for $n_0 = 3$ they are $x_1^{ms} \approx \pm 0.15h$, $x_2^{ms} \approx \pm 0.45h$, $x_3^{ms} \approx \pm 0.74h$.

The relaxation of $n_0 = 10$ dislocation pairs has been simulated using two different mesh sizes, $h / 100$ and $h / 160$. In both cases consistent behaviour has been observed. The positions of dislocations after relaxation differ insignificantly from the equidistant initial configuration. It is noteworthy that simulations with denser mesh give metastable equilibrium points that are slightly deeper toward the center in the film, and in particular with the head dislocations further away from the free surfaces. Thus, the metastability is not an artefact of the finite mesh size.

Since the decrease of the mesh-size does not lead to a significant change of the relaxation process, we simulate the cases of 11 through 18 dislocation pairs using the same mesh calculated for $n_0 = 20$ (the mesh size is $h / 320$). In the initial moment of time the 11, 12, ..., 18 dislocation pairs are again equidistantly distributed along the thickness of the film. Here again, all dislocations remain in the boundary and stop at metastable equilibrium points.

5.3.2. Case of $n_0 > 18$

In our study of larger numbers of dislocations – up to $n_0 = 40$ – we used the mesh size $h / 320$. A different behavior of dislocations has been found for this set of n_0 . The head dislocations pop out until the residual number of dislocation pairs is equal to 18. Thereafter, the remaining dislocations stop at the metastable equilibrium points x_i^{ms} , which are the same as for the case of $n_0 = 18$.

For the example of relaxation of a wall with initially $n_0 = 20$ dislocations, Fig. 7a illustrates the positions of all dislocations versus the dimensionless time τ (see Section 4). During the entire relaxation process (until all dislocations occupy metastable equilibrium points) a quasi-equidistant distribution of dislocations is maintained along the thickness of the film, with inter-dislocation spacing insignificantly reducing from the center of the film toward the surface. It is evident from Figure 7a that the egression of the head dislocations is accompanied by a disturbance and redistribution of the residual dislocations along the boundary length.

Figure 7b illustrates the positions of the head dislocations as a function of τ . At the beginning of the relaxation the leading dislocations climb to the center of the film (similar to compression of a spring) and afterwards the dislocation wall starts to expand. For the initial, 20 dislocation array the velocity of the leading dislocation is initially almost constant, increasing significantly only at a distance of $0.35h / 20$ from the surface. In the emerging array of 19 dislocations, the new leading dislocation initially slows down and then accelerates when it approaches the surface, again at $0.35h / 20$ from the surface. As it is seen in Figure 7b, the 19th head dislocation needs approximately 4-fold more time for reaching the surface compared the 20th dislocation. The behaviour is qualitatively changed for the 18th leading dislocation. As for the 19th dislocation, the climb is initially fast and then slows down. However, observation of the climb for extended periods of time shows a stationary dislocation geometry as opposed to egression. The simulation here suggests that a metastable equilibrium is reached where all relaxation stops.

The case of $n_0 = 20$ randomly distributed dislocation pairs has also been considered. Among all possible random distributions we have chosen one which satisfies the following two rules: (1) the spacing between neighboring dislocations should not be less than the mesh size $h / 320$; (2) the 20-th head dislocation should be at a distance not closer than $0.5h / 20$ from the surface. Otherwise, the proximity of the head dislocation to the free surface could significantly facilitate its egression. Several realizations of the random distribution have been investigated. Simulations have shown that at every realization the 20-th and 19-th head dislo-

cations faster reach the free surface and the remaining 18 dislocation pairs need more time to attain metastable equilibrium points as compared with the case of equidistant dislocation distribution.

Figure 8a shows the dependencies of the logarithm of the number of residual dislocation pairs n on the dimensionless time τ for four exemplary values of the initial dislocation number, $n_0 = 25, 30, 34, 40$. Even though the limited initial number does not allow a conclusive separation of regimes, one can still qualitatively discern a nearly linear stage, followed by a slower relaxation. In this respect, the phenomenology resembles the relaxation of disclination dipoles and quadrupoles in deformed polycrystals, cf. Refs. [35,36] with one exception, the initial fast relaxation stage is lacking. Not surprisingly, the data collapse onto a single ‘master curve’ when re-plotted with $t_f - t$ as the abscissa (Fig. 8b), where t_f , the full relaxation time, is the time until the 19-th dislocation egresses from the film. This shows that the relaxation rate depends on the current number of dislocations in a boundary, but not on the initial number of dislocations.

The dependence of t_f on the initial number of dislocation pairs is shown in Fig. 9. When plotted on a linear-log scale, a straight line is obtained at large n_0 . The linear law provides a good approximation for values of $n_0 > 22$. In terms of dimensionless time one obtains the empirical expression for the full relaxation time t_f of dislocation wall in the thin film:

$$\frac{t_f}{t_0} = -2.68 + 1.04 \ln(n_0) \quad (19)$$

In view of Eqn. (2), one finds that the relaxation time for a given film thickness is proportional to the logarithm of the misorientation angle,

$$\frac{t_f}{t_0} = -2.68 + 1.04 \ln\left(\frac{h\theta}{b_0}\right). \quad (20)$$

where t_0 is given by expression (17).

6. DISCUSSION AND CONCLUSIONS

6.1 Summary of results

We have inspected the energy and the relaxation behaviour of dislocation walls in a thin film of finite thickness, taking into account the boundary conditions for the dislocation stress fields at the free surface. Such walls represent small-angle tilt grain boundaries of finite size. The results are remarkable in two respects. When we start with a grain boundary containing many (up to 40) dislocations, we find that the dislocations migrate out of the boundary so that the misorientation decreases. A noteworthy finding is that the relaxation rate decreases as the boundary untilts. Even more remarkable is our finding that boundaries with fewer than 18 dislocations do not untilt any further. Instead, the dislocation array here relaxes towards a metastable state which is prevented from further relaxation by an energy barrier. We shall now discuss these results in the light of previous work.

6.2. Image forces

The observation of metastable states of boundaries with finite numbers of dislocations is at odds with the expectation that dislocations near a free surface are of necessity attracted to the surface by image forces. Our results suggest that this holds true for dislocations sufficiently close to the surface of the thin film. However, the results suggest a different picture for dislocations in the film interior. Here, the image forces act to let the dislocation climb away from the surface and towards a metastable position. In the case of a single dislocation, this position is in the center of the film, and the reversal of the climb force is found when the distance from the free surface is $\sim 1/4$ of the film thickness. As the number of dislocations is increased, the metastable configuration approaches an equidistant array as in a regular small-angle boundary. The trend for the outermost dislocations to be displaced inwards is progressively diminished as the number of dislocations increases.

The finding of metastable dislocation arrays deserves discussion, since the available studies agree that forces on dislocations near free surfaces are monotonically attractive to the free surface. As was already mentioned in Section 2.2, the image force on an edge dislocation near the surface of a half space is correctly described by the discrete image approach [31]. The attractive interaction is independently confirmed by analysis using a distribution of image dislocations along the surface [26,27], as in the present work. Since the stress field of a dislocation diminishes with the distance from the dislocation, the results for dislocations in a half space have implications for the thin film geometry in the limiting cases where the film is much thicker than the distance between the dislocation and the nearest surface. In that instance, the attractive behaviour of the surface must be recovered. The present results comply with that expectation in several respects. First, as displayed in Fig. 4, the image force of the half space is approached upon approach to the free surface. Second, as the film thickness, h , increases, the attractive outer regions of the film thicken in proportion to h . Third, the maximum repulsive force diminishes in magnitude as $1/h$. In other words, the classic picture of an overall attractive image force is recovered in the limit of a macroscopically thick film.

The existence of metastable states has a profound impact on small-angle tilt grain boundaries of finite size. Contrary to the expectation that these boundaries tend to untilt and thereby vanish through dislocation climb, our finding implies that the boundaries remain metastable and the grain rotation stops at finite misorientation. Equivalently, geometrically necessary dislocation walls that are created when a thin film undergoes plastic bending deformation may be trapped within the film. Those statements hold even when the atomic or vacancy mobility is high enough to enable the egression of the dislocations by climb towards the free surfaces.

6.3 Comparison to previous models of grain rotation

Our findings support Cahn's discussion of the relaxation rate: in spite of the Read-Shockley cusp in $\gamma(\theta)$, which appears to imply a divergence of the torque as the crystals rotate towards coincidence, the rotation rate actually slows down as the misorientation diminishes. This statement holds even when there are many dislocations and the grains still rotate. So far, our observations confirm similar statements in Refs. [4,37], derived with the help of conventional image force concepts. However, our more accurate computation shows that the rotation not only slows down, but that it stops altogether once the number of dislocations in the boundary drops to 18.

Our result of a rotation rate which scales with the grain size according to h^{-3} , when the climb of grain boundary dislocations is the rate-controlling process, is at variance with the h^{-4}

-law for $d\theta/dt$ of Refs. [4,13,14], which is essentially based on analysis of accommodation of the grain shape. The different scaling laws indicate that, at small grain size, the slower dislocation process replaces the faster accommodation as the rate-controlling step. It would then not be permitted to apply the h^{-4} scaling down to arbitrarily small sizes.

Our study is limited to tilt grain boundaries. In twist boundaries, which require more than one array of dislocations, the kinetics of rotation may be hindered by dislocation interactions. Ashkenazy and co-workers [23], inspecting the rotation of ‘twisted’ nanoclusters on single crystal substrates by molecular dynamics simulation, found that some boundaries do not untwist during the time-scale of the simulation, in spite of their extremely small size.

Our expression for the relaxation time can be used either for analysis of kinetics of rotation of nanoparticles on a substrate or for analysis of stability of grain and subgrain boundaries in thin metal films. It should be noted that results of the present paper are valid not only for small-angle grain boundaries whose structure can be described in the terms of discrete lattice and grain boundary dislocations. The results are also valid for high-angle grain boundaries vicinal to the special misorientations, since the structure of such boundaries can be described as a net of grain boundary dislocations imposed on the special grain boundary.

6.4 Comparison of relaxation rate to experiment

The present result has implications for the kinetics of rotation of nanoparticles on a substrate. We compare our results with the experimental data reported for the rotation of a single crystal Cu sphere, 200 μm in diameter, on a single crystal Cu substrate [9]. Annealing at 1323 K during 108 hours changed the misorientation angle from 81.6° to 74.4° . It was interpreted that the rotation occurs towards the high-coincidence $\Sigma=5$ high-angle grain boundary. The initial state represents a small-angle grain boundary with misorientation 7.85° , superimposed on the $\Sigma=5(73.75^\circ)$ high-angle grain boundary. Vacancy transport may here be dominated by grain boundary processes; our estimate of the time for untilting of the small-angle boundary therefore uses grain boundary diffusion constants from Ref. [38] ($\delta\mathcal{D}_b = 2.35 \times 10^{-14} \exp(-107.2 \text{ kJmol}^{-1} / RT) \text{ m}^3 \text{ s}^{-1}$), along with $G = 5.0 \times 10^4 \text{ MPa}$, the lattice parameter $a \approx 0.37 \text{ nm}$ and $\nu = 0.36$. The symbols R and T denote, respectively, the gas constant and the temperature. Assuming a neck size of half the sphere diameter, setting $b \approx 0.1 \text{ nm}$ and using Eqn. (15b) we obtain 55 hours. This approaches the experimental value reported in Ref [9] to within the factor of 2. In view of the various uncertainties in the experiment and of the approximate nature of our comparison, that may be taken as a good agreement.

Our simulations have shown that the relaxation rate decreases with decreasing the number of dislocations. Such a reduction of the relaxation rate on approaching critical misorientations (usually associated with an energy cusp) was observed experimentally [9,10].

Chan and Baluffi have reported that untilting of small gold crystallites occurred by climbing of grain boundary dislocations and during the climb process the spacing between grain boundary dislocations remained relatively uniform [12]. This is also in agreement with the observations of the present study.

6.5 Sinter neck versus internal boundary

Our simulation of a grain boundary bounded by free surfaces was motivated by comparison to experiments on grain rotation at sinter necks. It is of interest to consider, if and in how far the results are of relevance to grain rotation in a polycrystal, where boundaries end in triple lines joining them to other grain boundaries. In this regard it is noteworthy that the present results differ qualitatively with findings for the relaxation of disclination dipoles [35] and quadrupoles [36] in deformed polycrystals. Namely, all dislocations (dislocation pairs) composing a disclination dipole (quadrupole) are free to leave the original grain boundary independently on the initial number of dislocations [35,36]. This contrasts with the present geometry, where some dislocations are retained in boundaries bounded by free surfaces.

Differences are also found in the relaxation kinetics. The relaxation of disclination dipoles or quadrupoles involves three stages: the initial transient stage with the high relaxation rate; the metastable stage with the constant rate; the third final stage, when the relaxation rate quickly decreases [35,36]. Our simulations show that only the two last stages are present in the relaxation of the dislocation wall in thin film. The absence of the first transient stage may be related to the fact that the initial uniform distribution of dislocations along the boundary is maintained throughout the whole relaxation process, while the presence of the first stage in the relaxation of a disclination dipole or quadrupole is connected with rapid redistribution of dislocations from uniform to non-uniform distribution.

Grain boundaries in polycrystals end in triple lines that connect them to the adjacent boundaries. The stress state at these triple lines may not be adequately described by disclination dipoles or quadrupoles. Furthermore, grain rotation in polycrystals requires redistribution of matter by diffusive fluxes at a scale of the grain size. It is therefore not obvious in how far the present findings can be transferred to polycrystals.

7. SYNOPSIS

In summary, we have shown that the method of virtual image dislocations [28] affords an exact solution of the stress field of a small-angle grain boundary in a thin film. For the simplest geometries, namely one and two dislocations, we were able to integrate the work of creating the array and to thereby specify the specific grain boundary energy.

Our numerical simulation of the relaxation finds that, when starting out with a grain boundary containing many (up to 40) dislocations, the dislocations migrate out of the boundary with a relaxation rate that decreases as the boundary untilts. This is contrary to the behaviour expected based on the Read-Shockley cusp in the graph of boundary versus misorientation. Yet, our observation confirms similar statements in earlier papers [21,22]. It is also compatible with observations from atomistic computer simulation [23].

We find the rate of grain rotation which ensues from the relaxation to scale with the extension, h , of the boundary as h^{-3} . This is at variance with the rotation rate of polycrystalline grains, that has been given as scaling with h^{-4} [4,13,14].

Our most remarkable finding is that boundaries with fewer than 18 dislocations do not spontaneously untilt. Instead, the dislocation array here relaxes towards a metastable state in which the number of dislocations is conserved and where further untilting is prevented by an energy barrier. This observation is at odds with the expectation – based on exact solutions for image force near the surface of a half-space – of a monotonically attractive image force. Yet,

in the limit of a macroscopically thick film, our results converge towards the classic picture of an overall attractive image force.

Contrary to the expectation that small-angle grain boundaries tend to untilt and thereby vanish through dislocation climb, our finding implies that some finite-size grain boundaries remain metastable, with grain rotation arrested at a finite misorientation. Equivalently, geometrically necessary dislocation walls that are created when a thin film undergoes plastic bending deformation may be trapped within the film. Those statements hold even when the atomic or vacancy mobility is high enough to enable the egression of the dislocations by climb towards the free surfaces.

Acknowledgements – This work was supported by Deutsche Forschungsgemeinschaft (SFB 277 and Forschergruppe 714 ‘Plastizität in Nanokristallinen Metallen und Legierungen’). JW acknowledges John W. Cahn’s original suggestion to study this problem, during JW’s stay at NIST as a Humboldt Fellow in 1994.

REFERENCES

- [1] Hu H. Recovery and recrystallization of Metals. New York: Wiley; 1963. p. 311.
- [2] Doherty RD. Metal Sci 1974;8:132.
- [3] King AH, Harris KE. Mater Sci Forum 1996;204-206:355.
- [4] Harris KE, Singh VV, King AH. Acta Mater 1998;46:2623.
- [5] Klinger L, Rabkin E. Acta Mater. 2011;59:6691.
- [6] Shewmon PG. In: Recrystallisation, grain growth and textures. American society for metals. Ohio: Metals Park; 1966. p. 165.
- [7] Herrmann G, Gleiter H, Baero G. Acta Metall 1976;24:353.
- [8] Sautter H, Gleiter H, Baero G. Acta Metall 1977;25:467.
- [9] Kuhn H, Baero G, Gleiter H. Acta Metall 1979;27:959.
- [10] Mykura H. Acta Metal 1979;27:243.
- [11] Chan SW, Balluffi RW. Acta Metall 1985;33:1113.
- [12] Chan SW, Balluffi RW. Acta Metall 1986;34:2191.
- [13] Moldovan D, Wolf D, Philpot SR. Acta Mater 2001;49:3521.
- [14] Shan Z, Mao SX. Adv Eng Mater 2005;7:603.
- [15] Moldovan D, Wolf D, Phillpot SR, Haslam AJ. Acta Mater 2002;50:3397.
- [16] Cahn JW, Taylor JE. Acta Mater. 2004;52:4887.
- [17] Haslam AJ, Moldovan D, Yamakov V, Wolf D, Phillpot SR, Gleiter H. Acta Mater 2003;51:2097.
- [18] Markmann J, Bunzel P, Rösner H, Liu KW, Padmanabhan KA, Birringer R, Gleiter H, Weissmüller J. Scripta Mater 2003;49:637.
- [19] Shan Z, Mao SX. Adv Eng Mater 2005;7:603.

- [20] Read WT, Shockley W. *Phys Rev B* 1950;78:275.
- [21] Cahn JW. In: Handwerker CA, Blendell JE, Kaysser W, editors. *Sintering of advanced ceramics*. Westerville, Ohio: The American Ceramic Society, Inc.; 1990. p. 185–199.
- [22] King AH, Balasubramanian L. *Mater Sci Forum* 1995;189-190:143.
- [23] Ashkenazy Y, Averbach RS, Albe K. *Phys Rev B* 2001;64:205409.
- [24] Nabarro FRN, Kostlan EJ. *J Appl Phys* 1978;49:5445.
- [25] Siems R, Delavignette P, Amelinckx S. *Phys Stat Sol* 1962;2:421.
- [26] Jagannadham K, Marcinkowski MJ, *Phys Stat Solidi (a)* 1978;50:293.
- [27] Marcinkowski MJ, *Unified Theory of the Mechanical Behavior of Matter*, New York: Wiley 1979.
- [28] Gutkin MYu, Romanov AE. *Phys Stat Sol (a)* 1991;125:107.
- [29] Vladimirov VI, Kolesnikova AL, Romanov AE. *Phys Metals Metallogr* 1985;60:1106 (In Russian).
- [30] Weissmüller J, Markmann J, Grewer M, Birringer R. *Acta Mater* 2011;59:4366.
- [31] Hirth JP, Lothe J, *Theory of Dislocations*, 2-nd edition, New York: Wiley 1982.
- [32] Mura T. In: Herman H, editor. *Advances in material research*, vol. 3. New York: Interscience; 1968. p. 1–108.
- [33] Arzt E, Ashby MF, Verrall RA. *Acta Metall* 1983;31:1977.
- [34] Kaur I, Mishin Y, Gust W. *Fundamentals of grain and interphase boundary diffusion*. Chichester: Wiley 1995.
- [35] Nazarov AA. *Int Sci* 2000;8:315.
- [36] Bachurin DV, Nazarov AA. *Phil Mag* 2003;83:2653.
- [37] Martin G. *Phys Stat Sol (b)* 1992;172:121.
- [38] Kaur I, Gust W, Kozma L. *Handbook of grain boundary and interphase boundary diffusion data*. Stuttgart: Ziegler Press; 1989.

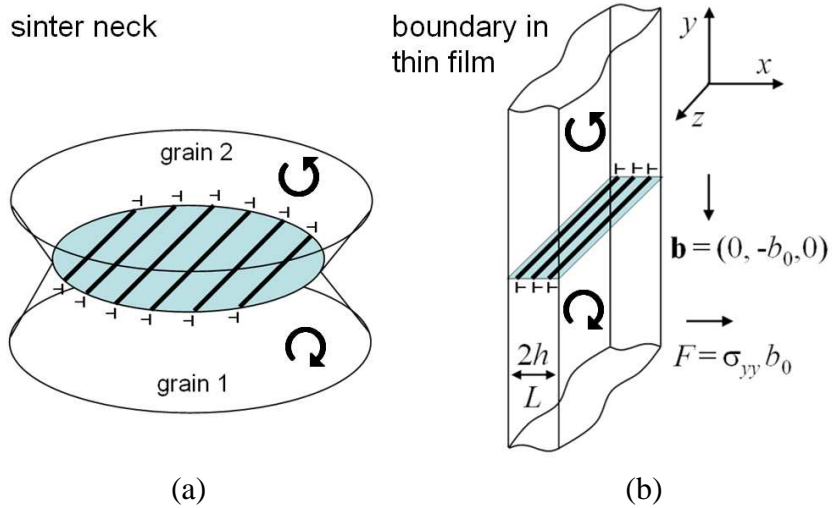


Fig. 1. Schematic illustration of dislocation arrays forming finite-size tilt grain boundaries. Arrows denote sense of rotation prompted by dislocation climb. (a) tilt boundary at a sinter neck. (b) geometry under investigation in this work. A thin film of thickness $L = 2h$ and of infinite extension in the two orthogonal directions (y, z) in the plane contains a small-angle tilt grain boundary (shaded). The normal to the boundary plane is in the plane of the film, aligned with the y -axis. The boundary is constituted by an array of parallel edge dislocations in the plane of the film, aligned with the z -axis. The Burgers vectors of magnitude b_0 are normal to the plane of the boundary and aligned with one of the directions (the y -axis) in the plane of the film. Climb forces tend to displace the dislocations in the boundary plane; these forces are of the form $F = \sigma_{yy} \cdot b_0$ (per line length of dislocation), with σ_{yy} a compressive or tensile stress component in the bulk, directed along the normal of the film.

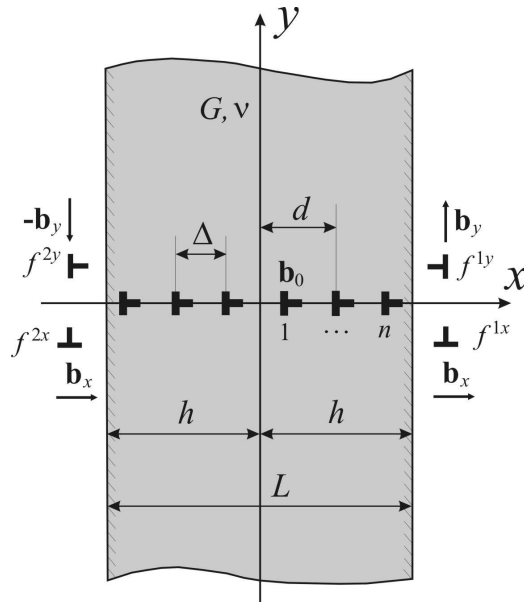


Fig. 2. Schematic representation of dislocation wall in a thin film, introducing the notation. Selected surface virtual dislocations are also shown.

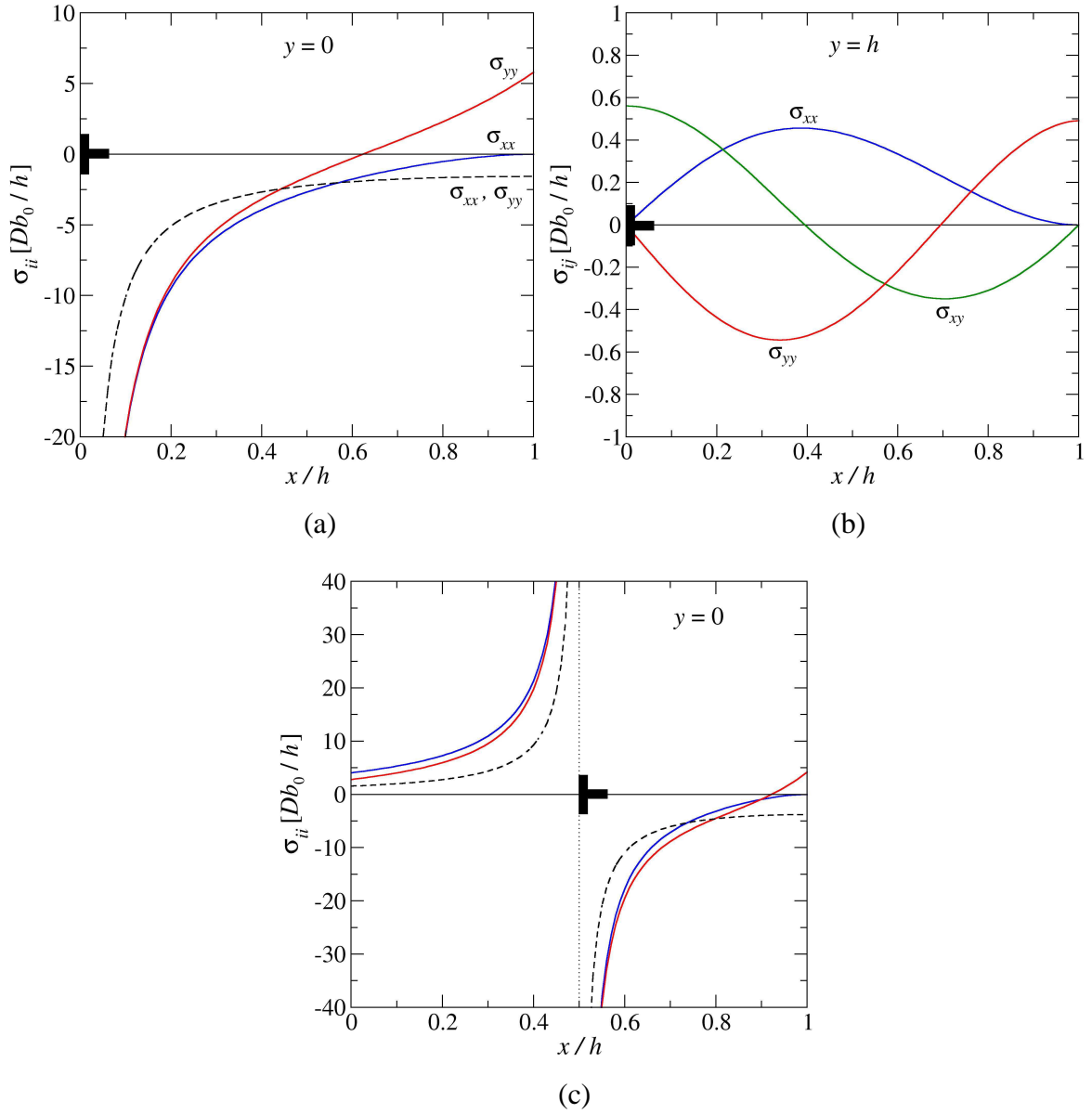


Fig. 3. Stress fields of a single dislocation, located in the centre of the film (a,b) of thickness h and halfway between the center and the outer surface (c). Ordinates: stress components σ_{xx} , σ_{yy} , or σ_{xy} , abscissas: normalized distance, x/h , from the centre of film. (a) and (c) show stresses in the plane containing the dislocation, $y = 0$, (b) shows stresses in the plane $y = h$. Position $x/h = 1$ refers to the right free surface. Solid curves are results of the present work; note that the boundary conditions $\sigma_{xx} = 0$, $\sigma_{xy} = 0$ are satisfied. Results for σ_{yy} , which need not vanish, are shown for comparison. Dashed curve in (a) refers to σ_{xx} and σ_{yy} (which are identical here) obtained from the discrete image dislocation method. Stress component σ_{xy} is zero in the plane $y = 0$ and therefore is not plotted in (a) and (c).

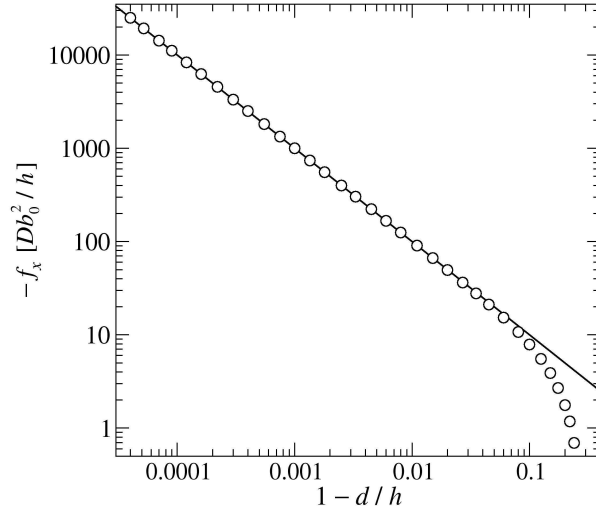


Figure 4: Climb force – as measured by the stress component σ_{yy} at the dislocation core – on a single dislocation versus the normalized distance, $1 - d/h$, from a free surface of the film. Dots: this work. Line: prediction of the classic image force approach for a dislocation near the surface of a half-space. Note agreement near the surface and deviation in the interior of the film.

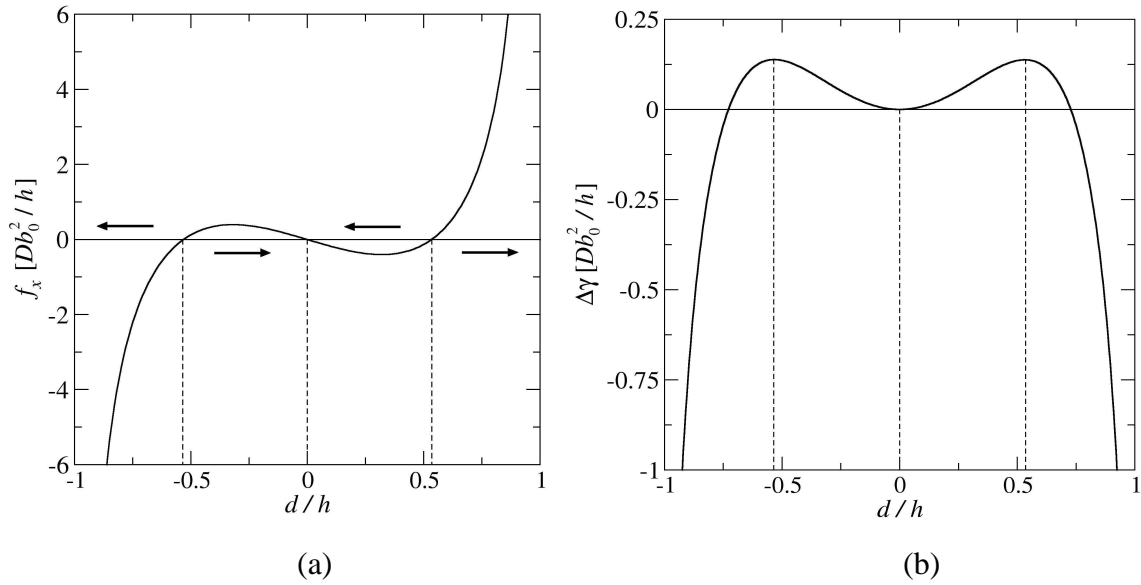


Fig. 5. (a) Climb force, $f_x = -b_0 \sigma_{yy}$, on a single dislocation in a thin film of thickness $L = 2h$ as the function of the distance, d , of the dislocation from the central plane of the film. The force represents the image stresses of the dislocation from the two surfaces. Arrows denote direction of climb. Dislocations located in the outer parts of the film are attracted to the surface, while dislocations closer than roughly $h/2$ to the central plane of the film tend to climb spontaneously to a metastable position in the central plane. (b) Elastic energy per unit length as the function of the dislocation position. Energy is specified as an effective excess in specific grain boundary energy, $\Delta\gamma$, defined as the excess (relative to the metastable state) in elastic strain energy per area of boundary. Vertical dashed lines in (a) and (b) emphasize metastable and unstable equilibrium positions. Specification of σ and $\Delta\gamma$ is in reduced units, where the symbols have the following meaning: $D = G/4\pi(1-\nu)$, b_0 - Burgers vector of the dislocation, h - half-thickness of the film.

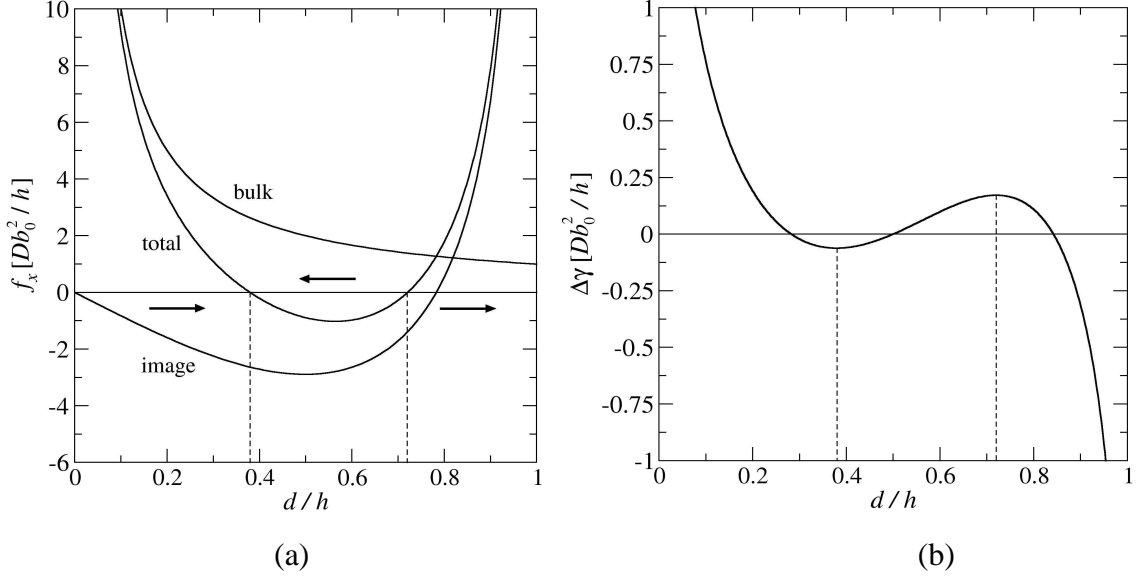


Fig. 6. Similar to Fig. 4, but for the case of two symmetric dislocations ($n_0 = 1$) located at positions $+d$ and $-d$. Climb force, $f_x = -b_0 \sigma_{yy}$, at the dislocation position d (a) and elastic energy per unit length of the film (b) as the function of d . In (a), the total stress as well as the contributions from the image dislocations and from the conventional bulk stress field are shown separately, as indicated by labels in the figure. Vertical dashed lines in (a) and (b) emphasize metastable and unstable equilibrium positions. See caption of Fig. 4 for explanation of labels.

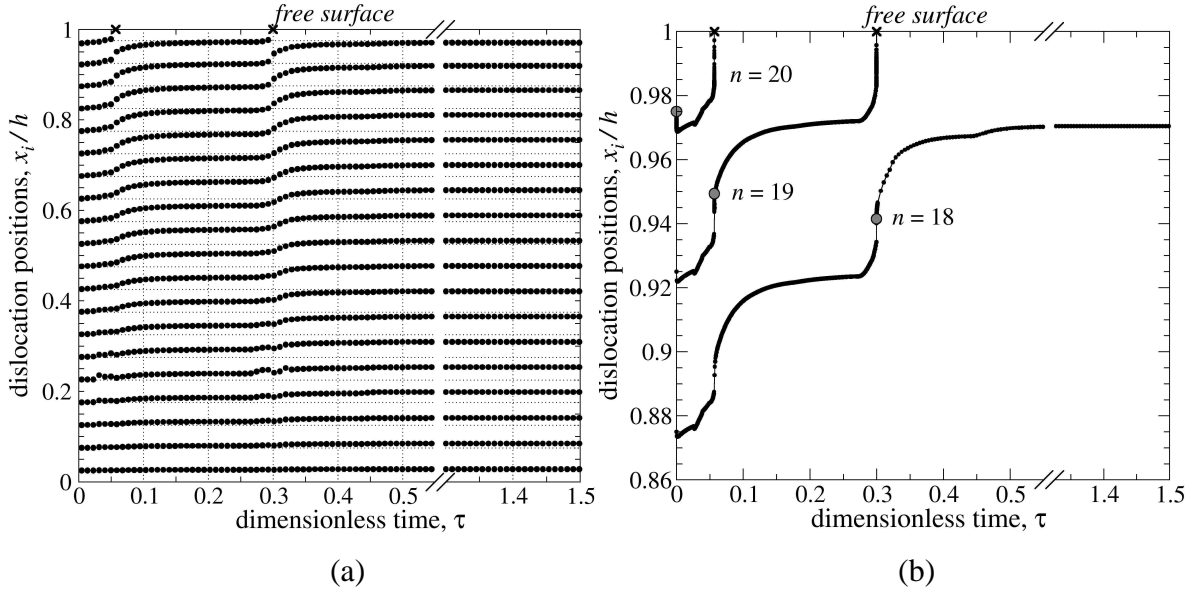


Fig. 7. (a) Dislocation positions x_i/h as a function of dimensionless time τ . Horizontal dashed lines indicate the initial positions of the dislocations in the wall. Two crosses show the times at which the 20-th and the 19-th head dislocation pairs have reached the free surfaces; (b) detailed illustration of the position of the 20-th, 19-th and 18-th dislocations as a function of τ . The gray dots are the initial positions of the head dislocations. Note axis break on abscissa, emphasizing the stationary state of the array with 18 dislocations.

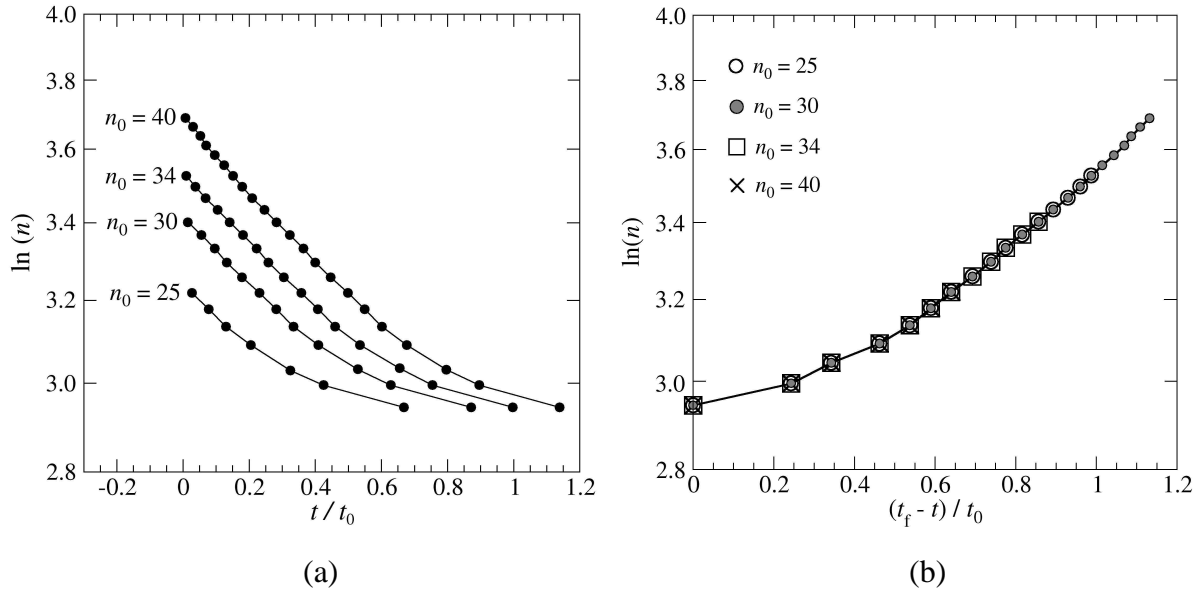


Fig. 8. Illustration of the kinetics of the relaxation. Symbols refer to the instants t at which individual dislocation pairs meet the surface and pop out, leaving n pairs in the boundary. Thus, the last pair has vanished and coincidence reached at the point in time, where $n = 18$. Graphs are for various values n_0 . Lines interpolating the data points are guides to the eye. The graph of $\ln(n)$ versus t/t_0 in part (a) illustrates that the relaxation rate slows down as the boundary untilts. Part (b): same data, plotted with $(t_f - t)/t_0$ as the abscissa.

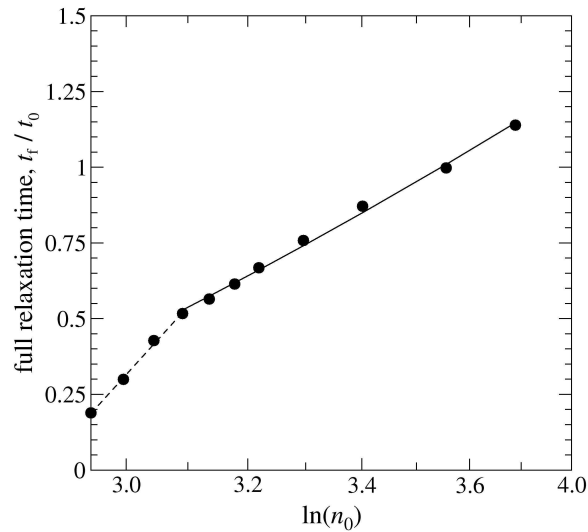


Fig. 9. Full relaxation time, t_f/t_0 , versus initial number, n_0 , of dislocation pairs. Note that t_f/t_0 is defined as the time interval until the last – i.e., the 19-th – dislocation pops out.